ACS APPLIED ENERGY MATERIALS

Pyridine-Containing Polyhydroxyalkylation-Based Polymers for Use in Vanadium Redox Flow Batteries

Julian Stonawski,* Melanie Schroeder, Janett Gördes, Frieder Junginger, Linus Hager, Pascal Lauf, Muhammad Mara Ikhsan, Dirk Henkensmeier,* Simon Thiele, and Jochen Kerres

Cite This: *ACS Appl. Energy Mater.* 2024, 7, 10834−10845

Read Online

ACCESS | Metrics & More | Article Recommendations | Supporting Information

ABSTRACT: In this work, a class of polymers with pendant pyridine moieties and variable *p*-terphenyl (pTP) content was developed via superacid catalyzed polyhydroxyalkylation (PHA). High controllability of the copolymer composition was demonstrated, allowing for straightforward fine-tuning of the material properties. Low levels of *p*-terphenyl were used to obtain materials with improved conductivities of up to 83 mS cm^{-1} in 3 M H_2SO_4, allowing the efficient application at high current densities. Increasing the *p*-terphenyl content significantly improved the selectivities up to 1.88 × 10^{13} S s m^{-3}, resulting in optimized materials for low current density applications. A single cell equipped with BP-pTP10-Py exhibited an energy efficiency (EE) of 76.7% at a current density of 200 mA cm^{-2} (vs 73.7% for the commercial reference FAPQ330). At lower current density (50 mA cm^{-2}), the single cells equipped with BP-pTP20-Py and BP-pTP35-Py showed the highest EE of 92.3% (vs 90.9% for the FAPQ330). Ex situ stability tests in 1.6 M V(V)/2 M H_2SO_4 proved high chemical stability with no changes in the NMR spectra and similar V(IV) contents in the stability solution as the reference FAPQ330. In addition, long-term in situ tests revealed no evidence of performance degradation for the single cell equipped with BP-pTP20-Py.

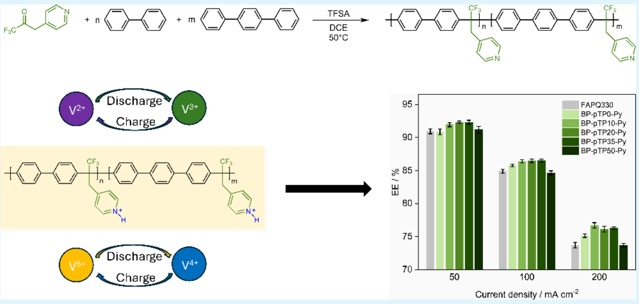

KEYWORDS: *Polyhydroxyalkylation, pyridine-containing, ion-selective membrane, improved selectivity, vanadium redox flow battery*

1. INTRODUCTION

The recent trend toward renewable energies requires reliable energy storage technologies to account for the intermittency of wind and solar power and the associated stabilization of the power grid.[1,2] Among these technologies, Redox Flow Batteries (RFB) gained significant attention due to their high cycling stability and the decoupling of power and capacity, allowing a cost-efficient capacity scaling and electrolyte replacement.[3] Next to organic redox systems,[4] several inorganic redox flow chemistries like zinc-vanadium,[5] all-vanadium,[6] and iron−chromium[7] are investigated, whereas the all-vanadium system is most extensively studied. The fact that the vanadium redox flow battery (VRFB) utilizes only one element leads to the advantage of reduced maintenance costs due to crossover, as the capacity decay can be restored by electrolyte rebalancing. This is not feasible in the case of unsymmetric chemistries using different elements as analyte and catholyte.[8] One key factor for a VRFB's performance is the separator between the two half-cells, which can either be a porous material or a dense ion-exchange polymer.[9,10] Suitable materials should show high H^+/V selectivity, stability against the electrolyte, and sufficient mechanical strength.[11,12] The commercially available membrane FAPQ330 by FUMATECH BWT GmbH exhibits good H^+/V selectivity and conductivity.[13] To further increase the performance of VRFB systems, current research aims to develop new materials showing comparable or higher H^+/V selectivity, higher conductivity, and sufficient stability against V(V) species. Recently, different materials such as sulfonated polyimides,[14] supramolecular patched Nafion,[15] or zwitterionic poly(terphenylene piperidinium)[16] were developed. Among all new materials, especially materials containing nonquaternized amine or (benz)imidazole moieties were shown to be promising.[17−20] Zhang et al., for example, developed a chemically stable cross-linked pyridine-containing material based on an aromatic backbone, where wide ion transport channels were formed by preswelling in H_3PO_4 at different temperatures.[21]

In 2001, a new polymerization technique, polyhydroxyalkylation (PHA), was reported by Colquhoun, leading to linear high molecular weight polymers by the reaction of activated ketones with aromatic compounds in superacidic media.[22]

Received: July 1, 2024
Revised: November 9, 2024
Accepted: November 15, 2024
Published: November 21, 2024

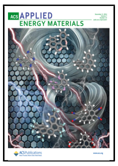

Since then, many new polymer structures with various backbones and functionalities have been developed.[23−25] Based on this reaction, Mu et al. synthesized aromatic pyridine-and imidazole-containing polymers by reacting *p*-terphenyl and acetylpyridine or methyl-2-imidazolecarboxaldehyde in trifluoromethanesulfonic acid (TFSA). In addition, anion-exchange groups were implemented into the imidazole-containing polymer structure by functionalizing the non-alkylated nitrogen with a quaternary ammonium-containing side chain. The membranes showed decent mechanical properties, promising performance in single-cell VRFB tests, and sufficient chemical stability when immersed for 400 h in a V(V)-electrolyte. However, despite the better conductivity and permeability of the anion-exchange-group-containing polymers, the voltage efficiency was still relatively low compared to other reported membrane systems. This can be related to the high resistance of the membrane due to the high molar ratio of aromatic rings to functional groups and the low mobility of the functional group due to direct attachment to the backbone.[11,24]

In this work, we synthesized a series of new pyridine-containing aromatic (co)polymers via PHA of 1,1,1-trifluoro-3-(pyridin-4-yl)propane-2-one and biphenyl or both, *p*-terphenyl and biphenyl. The design of the material aimed at optimizing conductivity while maintaining selectivity without the necessity of any pretreatment of the membranes prior to the use in the VRFB. For this, the following two features were implemented into the polymer structure. First, the amount of *p*-terphenyl in the polymer structure was reduced by increasing the amount of biphenyl, promoting overall acid uptake without any preswelling steps due to the decreasing ratio of aromatic moieties to functional groups. Second, the pyridine moiety was attached to the backbone via a short C1 spacer to create a rotational axis and slightly increase the mobility of the ion exchange group. It is well-known that a spacer between the ion-conducting group and the backbone could promote phase separation and increase conductivity, which becomes more pronounced with increasing side chain length.[26,27] However, in VRFB membranes, the phase separation should not be too strong as it can negatively affect the selectivity if the diameter of the ion transport channels exceeds the size of the hydrated vanadium species of 0.7 nm.[28] The greater distance of the pyridine moiety to the carbonyl group necessitated the introduction of a CF_3 group into the monomer to sufficiently activate the carbonyl group for the PHA. The resulting materials showed sufficient molecular weights to form stable and flexible films and were soluble in common organic solvents such as DMSO, DMAc, and NMP. Different ratios of biphenyl and *p*-terphenyl were incorporated into the structure. This approach obtained a broad material range regarding conductivity, acid uptake, V(IV)-crossover, and tensile properties. In addition to the ex-situ characterization, the materials were characterized electrochemically in VRFB single-cell tests.

2. EXPERIMENTAL SECTION

2.1. Materials. Perfluoroacetic anhydride, dry toluene, 4-methylpyridine, pyridine, potassium carbonate, dry dichloroethane (DCE), trifluoromethanesulfonic acid (TFSA), trifluoroacetic acid (TFA), biphenyl (BP), *p*-terphenyl, *N*-methylpyrrolidone (NMP), conc. hydrochloric acid (HCl), ethyl acetate, and isopropanol were purchased from Sigma-Aldrich. Vanadium(IV) oxide sulfate hydrate ($VOSO_4$ x 3 H_2O) was purchased from TCI chemicals, 0.01 M HCl standard solution, 0.01 M sodium hydroxide standard solution (NaOH), concentrated sulfuric acid (H_2SO_4), and anhydrous magnesium sulfate ($MgSO_4$) were purchased from Daejung Chemicals & Metals Co., Ltd., FAPQ330 membranes were provided by FUMATECH BWT GmbH. The vanadium electrolyte (1.6 M V(III/IV) in 2 M H_2SO_4) was purchased from GfE Metalle and Materialien GmbH. The thermally activated polyacrylonitrile-based carbon felts (SIGRACELL GFD 4.65 EA) were provided by SGL CARBON GmbH. All chemicals and materials were used without further purification.

2.2. Synthesis of 1,1,1-Trifluoro-3-(pyridin-4-yl)propan-2-one. The synthesis of 1,1,1-trifluoro-3-(pyridine-4-yl)propane-2-one was performed according to a modified literature protocol.[29] 4-methylpyridine (0.32 mol, 31.5 mL, 1.00 equiv) and pyridine (1.60 mol, 129 mL, 5.00 equiv) were dissolved in 830 mL anhydrous benzene and cooled to 0 °C. Perfluoroacetic anhydride (0.96 moL, 134 mL, 3.00 equiv) was added dropwise within 90 min. After stirring for 25.5 h at room temperature (RT), aqueous 2 M K_2CO_3 solution (500 mL) was added slowly. The precipitate was filtered off, the organic and aqueous phases were separated with a separation funnel, and the organic phase was dried under vacuum. After adding ethyl acetate (50 mL), the nondissolved portion was filtered off and recrystallized from ethyl acetate (isolated yield: 18%).

2.3. Synthesis of Poly(biphenyl-*co*-(*p*-terphenyl)-*co*-1,1,1-trifluoro-3-(pyridine-4-yl)propane-2-one). The synthesis of poly(biphenyl-*co*-(*p*-terphenyl)-*co*-1,1,1-trifluoro-3-(pyridine-4-yl)-propane-2-one) was performed following a typical procedure used for PHAs with small modifications.[30] As an example, the preparation of poly(biphenyl-*co*-(1,1,1-trifluoro-3-(pyridin-4-yl)propane-2-one) is given. At RT, biphenyl (12.2 mmol, 1.88 g, 1.00 equiv), 1,1,1-trifluoro-3-(pyridine-4-yl)propane-2-one (15.9 mmol, 3.00 g, 1.30 equiv) and dry dichloroethane (13.4 mL) were stirred in a 100 mL Schlenk flask. After cooling to 0 °C, TFSA (150.08 mmol, 13.4 mL 11.7 equiv) was added to the mixture within 2 min. Subsequently, the mixture was heated to 50 °C and allowed to react for 15 days. The viscous solution was precipitated into deionized water (400 mL), and the polymer was collected by filtration. The polymer was dissolved in NMP (40 mL), precipitated into isopropanol (500 mL), and again separated by filtration. Finally, the product was dried at 85 °C for 24 h.

2.4. Membrane Preparation. An appropriate amount of the polymer was dissolved in NMP to yield a concentration between 23 and 30 wt %. After complete dissolution, the polymer solution was filtered through a thin layer of cotton wool. A thin film was cast on a glass plate using a doctor blade. Subsequently, the NMP was evaporated for 2 h at 110 °C, and the resulting polymer film was detached by immersing the glass plate into water. The membranes were treated 3x with 1 M HCl at 85 °C, 1x with 0.5 M K_2CO_3 at 85 °C, and 1x with DI-water at 85 °C. Finally, the membranes were dried at 85 °C for 24 h.

2.5. Polymer and Membrane Characterization. *2.5.1. ^1H NMR.* ^1H NMR measurements were performed on a 500 MHz JEOL JNM-ECZ-500R at room temperature using deuterated solvents. The spectra analysis was performed using the software MestReNova (V. 14.2.0−26256).

2.5.2. Thermogravimetric Analysis. Thermogravimetric analysis was performed on a TGA 800 by PerkinElmer under a synthetic air atmosphere between 25 and 900 °C with a heating rate of 20 K min^{-1} to evaluate the materials' thermal stability. The derivation of the thermograms and deconvolution of the peaks were performed with Origin 2020.

2.5.3. Gel Permeation Chromatography. Determination of molecular weight distributions was performed on a SECcurity^2 1260 by PSS equipped with a PSS GRAM guard column and three separation columns (1x PSS GRAM 10 μm 100 Å and 2x PSS GRAM 10 μm 3000 Å). Chromatography grade NMP with 0.1 M LiBr was used as the eluent. Measurements were performed with a flow rate of 1.0 mL min^{-1} at 70 °C. A dual variable wavelength UV−vis (P/N 404−2107, PSS) and a refractive index detector (P/N 404−2106, PSS) were used for detection. Polystyrene standards from PSS were used to calibrate the system.

2.5.4. Scanning Electron Microscopy. Scanning electron microscopy (SEM) images were taken on a TESCAN VEGA3 with an acceleration voltage of 20 kV using a secondary electron detector. Before the measurement, the samples were adhered to an aluminum sample stub using conductive carbon tape and sputter-coated with platinum.

2.5.5. Acid-Uptake and -Concentration. Acid uptake of the membranes was analyzed by weighing 1 cm × 4 cm pieces to get the dry weight m_{dry} and immersing them into 3 M H_2SO_4 at RT for 48 h. The samples were blotted with SCIENCE Wipers Small from KIMTECH and weighed to receive the wet weight m_{wet}. Afterward, the samples were immersed into 20 mL 0.01 M NaOH for 24 h to neutralize all absorbed sulfuric acid. The membrane samples were taken out and rinsed with water, and the remaining NaOH was titrated with 0.01 M HCl using a Metrohm 848 Titrino Plus and an Ecotrode Plus (6.0262.100). By using the following equations, the acid uptake (AU%), the acid doping level (ADL), and the acid concentration c_{H2SO4} were calculated, where m_{wet} and m_{dry} are the wet and dry weights of the membrane, respectively, n_{Pyr} is the number of pyridine units, n_{H2SO4} the amount of absorbed sulfuric acid, M_{H2SO4} the molecular weight of sulfuric acid, σ_w the density of the sulfuric acid at the respective mass fraction and $m_{H2SO4,\ free}$ and m_{H2O} the masses of the free sulfuric acid and water, respectively. The measurements were performed with five separate samples per membrane type. Acid concentration measurements were not performed for the FAPQ330 as the membrane turned black directly after immersion in 0.01 M NaOH.

$$\mathrm{AU\%} = \frac{m_{\mathrm{wet}} - m_{\mathrm{dry}}}{m_{\mathrm{dry}}} \tag{1}$$

$$\mathrm{ADL} = \frac{n_{\mathrm{H_2SO_4}}}{n_{\mathrm{Pyr}}} \tag{2}$$

$$c_{\mathrm{H_2SO_4}} = \frac{(n_{\mathrm{H_2SO_4}} - n_{\mathrm{Pyr}})}{\left(\frac{(n_{\mathrm{H_2SO_4}} - n_{\mathrm{Pyr}}) \times M_{\mathrm{H_2SO_4}} + m_{\mathrm{H_2O}}}{\sigma_{\mathrm{w}}}\right)} \tag{3}$$

2.5.6. Swelling Properties. The same 1 cm × 4 cm pieces used to determine the acid uptake properties were used to determine the swelling properties. Thicknesses of the dry and the wet membranes, d_{dry} and $d_{wet,}$ respectively, were measured with an ABS Digital Thickness Gauge 547−526S by Mitutoyo. Pictures were taken at the same distance before and after immersing the membrane pieces into 3 M H_2SO_4 with document camera K1000 (Nanjing Chengben Electronic Technology Co., Ltd.) to receive the length and width percentage change. The pictures were analyzed for the number of pixels with the software ImageJ to gain dry (l_{dry}) and wet (l_{wet}) length and dry (w_{dry}) and wet (w_{wet}) width. Thickness swelling S_{Th} and area swelling S_A were calculated with the following equations, in which d_{wet} and d_{dry} are the wet and dry thicknesses, respectively.

$$S_{\mathrm{Th}}\% = \frac{d_{\mathrm{wet}} - d_{\mathrm{dry}}}{d_{\mathrm{dry}}} \times 100\% \tag{4}$$

$$S_{\mathrm{A}}\% = \frac{l_{\mathrm{wet}} \times w_{\mathrm{wet}} - l_{\mathrm{dry}} \times w_{\mathrm{dry}}}{l_{\mathrm{dry}} \times w_{\mathrm{dry}}} \times 100\% \tag{5}$$

2.5.7. Conductivity. Conductivities of the membranes were measured by through-plane impedance spectroscopy utilizing a Zive SP1 potentiostat within a frequency range of 500 kHz to 30 kHz and an amplitude of 0.1 mV in a custom-made cell with an active electrode area of A = 1.767 cm^2. For every membrane type, three pieces were immersed in 3 M H_2SO_4 or 1.5 M $VOSO_4$/3 M H_2SO_4 for 48 h prior to the measurement, and the thickness of each sample was measured with an ABS Digital Thickness Gauge 547−526S by Mitutoyo. The resistance R of the cell was determined for one, two, and three stacked samples by setting it equal to the real part of the impedance at the frequency where the imaginary part of the impedance is zero. The stack resistance values were plotted against the thickness of the stack, and the slope of the linear fit through these three points was set as the thickness-normalized resistance R_N. The conductivity σ was calculated with the following equation.

$$\sigma = \frac{1}{R_{\mathrm{N}} \times A} \tag{6}$$

2.5.8. V(IV) Permeability. V(IV) permeation tests were performed in an H-cell with an active area of A = 4.75 cm^2 at RT. The dry membrane pieces were clamped between the two compartments of the cell. One side was filled with 15 mL C_V = 1.5 M V(IV)/3 M H_2SO_4 and the other with V_M = 120 mL − 130 mL 1.5 M $MgSO_4$/3 M H_2SO_4. During the testing procedure, both solutions were stirred to prevent the buildup of any concentration gradients. After specific time intervals, samples were taken from the $MgSO_4$ side, and the V(IV) concentration was determined using the UV−vis spectrometer Cary100 UV−vis (Agilent Technologies) at a wavelength of 762 nm. Four samples were taken for every measurement, and the V(IV) concentration at the Magnesium sulfate side $C_{VM(IV)}$ was plotted against the time t. A linear regression analysis through at least four points was used, and the slope $\left(\frac{dC_{V_{M(IV)}}}{dt}\right)$ of the fitted curve was used to calculate the V(IV) permeability $P_{V(IV)}$. The membrane's wet thickness L_w was directly measured after disassembling the cell. Subsequently, the V(IV) permeability was calculated using the following equation.

$$P_{\mathrm{V(IV)}} = \frac{1}{C_{\mathrm{V}}}\left(\frac{dC_{V_{\mathrm{M}}(\mathrm{IV})}}{dt}\right)\left(\frac{L_{\mathrm{w}}V_{\mathrm{M}}}{A}\right) \tag{7}$$

2.5.9. Ex Situ Stability in V(V). To test the material's ex-situ stability, samples of FAPQ330, BP-pTP0-Py, and BP-pTP50-Py were immersed in 1.6 M V(V)/2 M H_2SO_4 for 66 days at RT (around 150 mg in 5 mL solution). Subsequently, the concentration of V(IV) per g of polymer in the solution, the molecular weight distribution, and the ^1H NMR spectra of the polymers were analyzed.

2.5.10. Tensile Tests. Tensile tests were performed with the Tensile Testing Machine QC-508E by Cometech Testing Machines Co., Ltd. at a test speed of 10 mm min^{-1}, a temperature of 23 °C and 61% relative humidity. Five 1 cm × 4 cm pieces were immersed in 3 M H_2SO_4 before the test for each membrane.

2.5.11. VRFB Single-Cell Tests. VRFB single-cell tests were performed with a single cell with an active area of 24 cm^2. Thermally activated carbon thick felt electrodes were used and compressed to 80% of their original thickness. 50 mL of electrolyte (1.6 M V(III/IV) in 2 M H_2SO_4) was used on both sides and inerted with argon (const. flow) for the duration of the cell testing. The electrolyte was pumped through the system with a flow rate of 20 mL min^{-1} and stirred during the battery testing. The electrolyte was initially charged to SOC = 20% with constant current (cc) at 20 mA cm^{-2}. Afterward, ten constant current (cc) cycles were each performed at 50 mA cm^{-2}, 100 mA cm^{-2}, and 200 mA cm^{-2}. Before and after ten cc cycles, UI curves (0, 5, 10, 20, 30, 40, 50, and 60 mA cm^{-2}) were measured at SOC = 50% to determine the area-specific resistance (ASR). Cycling tests (50 constant current cycles at 100 mA cm^{-2}) were performed under the same conditions, with the addition of a hydraulic shunt connection between the tanks to level differences due to volume crossover. The CE, VE, and EE were calculated using the following equations, where I_d is the discharge current, I_c is the charge current, V_d is the discharge voltage, V_c is the charge voltage, and t is the time.

$$\mathrm{CE}\ (\%) = \frac{\int I_{\mathrm{d}}\ \mathrm{d}t}{\int I_{\mathrm{c}}\ \mathrm{d}t} \times 100\% \tag{9}$$

$$\mathrm{EE}\ (\%) = \frac{\int V_{\mathrm{d}} I_{\mathrm{d}}\ \mathrm{d}t}{\int V_{\mathrm{c}} I_{\mathrm{c}}\ \mathrm{d}t} \times 100\% \tag{10}$$

$$\mathrm{VE}\ (\%) = \frac{\mathrm{EE}}{\mathrm{CE}} \times 100\% \tag{11}$$

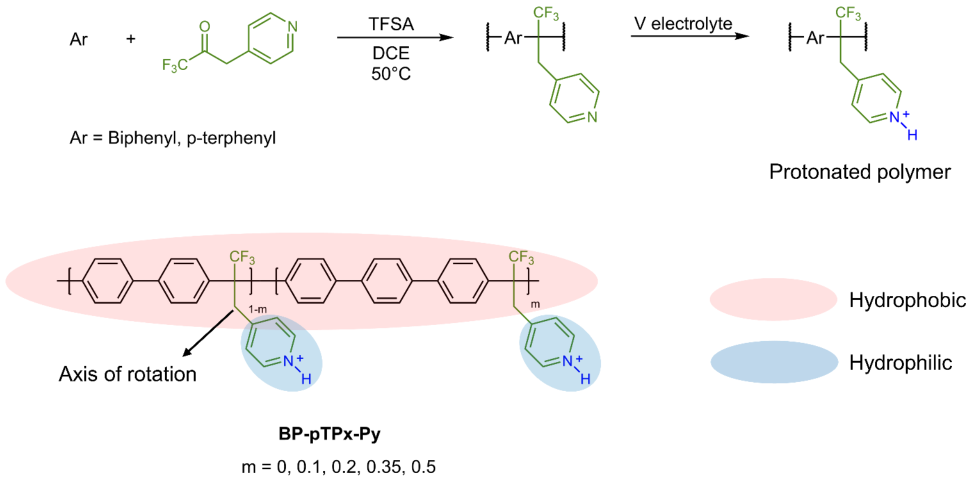

Figure 1. Schematic representation of the BP-pTPx-Py polymer synthesis and protonation step in the acidic V-electrolyte. Hydrophobic parts are accentuated in light red and hydrophilic parts in light blue. The variable *m* represents the mole fraction of *p*-terphenyl based on the total amount of biphenyl and *p*-terphenyl.

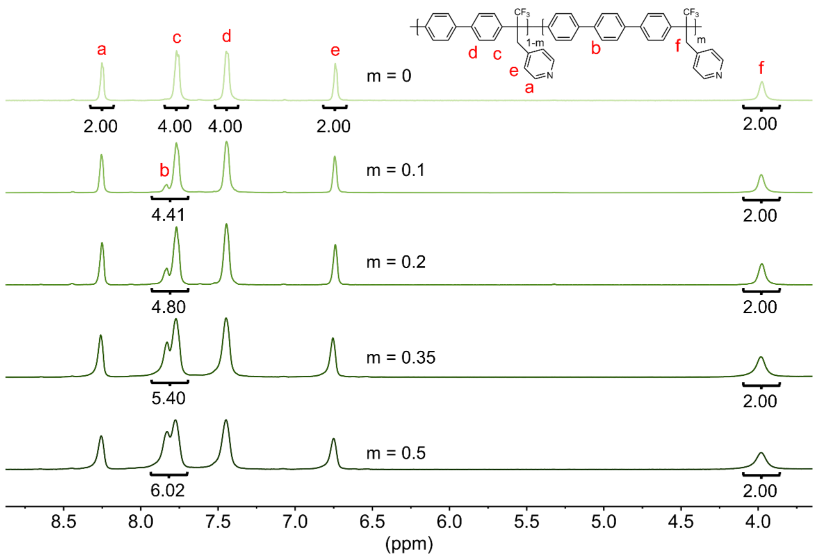

Figure 2. ^{1}H NMR spectra of BP-pTPx-Py polymers with increasing molar fractions of *p*-terphenyl (increasing *m* values). The proton signals of the middle ring in the *p*-terphenyl moiety (signal b) appear at around 7.8 ppm and increase with increasing amounts of *p*-terphenyl. The integral quotient of the signals in the range between 7.7 and 8.0 ppm (signal b+c) and the signal at around 4.0 ppm (signal f) were used to calculate the amount of *p*-terphenyl present in the polymer structure.

2.5.12. VRFB Self-Discharge Single-Cell Tests. VRFB self-discharge tests were performed in a Scribner 857 RFB test system with a Scribner single-cell with an active area of 5 cm^2, squared patterned, and a serpentine flow field at room temperature of 20 to 21 °C. Thermally activated carbon felts with a thickness of 4.6 mm from SGL carbon, compressed to 3.22 mm (70% of their original thickness), were used as electrodes. Twenty-five mL of electrolyte (1.6 M V(III/IV) in 2 M H_2SO_4) was used for both sides. The electrolyte was stirred and inerted with a constant flow of humidified nitrogen into the headspace of the vessels and charged to an open circuit voltage (OCV) of 1.33 V (SOC = 20%) with a constant current of 20 mA cm^{-2} and pumped with a flow of 30 mL min^{-1}. For the SOC tracking, a SOC cell from Scribner was placed in the electrolyte flow after the vessels and before the active cell. After reaching SOC = 20%, the electrolyte flow was stopped to measure the battery cell voltage under static conditions until dropping to 0.9 V.

3. RESULTS AND DISCUSSION

3.1. Polymer Synthesis and Membrane Preparation.

In recent years, several new polymer structures were synthesized by PHA reactions, which generally consist of the reaction of an activated carbonyl compound and an aromatic structure catalyzed by a superacid like trifluoromethanesulfonic acid.[31] The thus prepared structures show sufficient mechanical strength and a variety of functional groups can be implemented by varying the monomers. Additionally, high chemical stability in the oxidizing V(V) environment was reported.[32−34] Several research groups have already reported materials with pyridine as the functional group, which showed excellent performance and stability of the functional group.[19,21] For example, Mu et al. reported a well-performing system based on the polyhydroxyalkylation of 4-acetylpyridine and *p*-terphenyl. Nevertheless, the voltage efficiency, which is strongly connected to the resistance of the membrane, can still be optimized. For example, the conductivity of ion exchange membranes can be increased by raising the IEC,[35] changing the membrane morphology,[20] or attaching the ion-conducting group on a side chain.[36]

Based on the previous statements, we developed a new pyridine-containing polymer system utilizing a straightforward PHA, with the functional group being separated from the backbone by a C1 spacer. To control the physical properties of the polymers the IEC and hydrophobicity were altered by implementing different amounts of biphenyl and *p*-terphenyl into the backbone. The schematic representation of the system, including the representation of hydrophilic and hydrophobic sections, is shown in Figure 1.

A series of five different polymers was synthesized. ^1H NMR measurements confirmed the structure of the polymers and the amount of *p*-terphenyl. Figure 2 shows the spectra of BP-pTPx-Py polymers with increasing pTP content from top to bottom.

As can be seen from Figure 2, all expected signals for the structure can be found in the spectra. The signal at 7.78 ppm is not apparent in the spectra for BP-pTP0-Py as it can be assigned to the protons of the middle ring of the *p*-terphenyl unit. By comparing the integral of the signals belonging to the protons in the pyridine unit to the integral of the other aromatic protons, the actual amount of *p*-terphenyl was determined. Table 1 summarizes the amount of *p*-terphenyl in the feed and the measured amounts in the resulting polymer.

Table 1. Polymer Composition, M_w, and PDI of the Synthesized BP-pTPx-Py Polymers

polymer	pTP feed [mol %]	pTP NMR [mol %]	M_w [kDa]	PDI
BP-pTP0-Py	0	0	42	1.6
BP-pTP10-Py	10	10	40	1.6
BP-pTP20-Py	20	20	53	1.6
BP-pTP35-Py	35	35	55	1.6
BP-pTP50-Py	50	50	48	1.6

^1H NMR spectra revealed that the amount of *p*-terphenyl in the polymer structure equals the amount of *p*-terphenyl in the monomer feed for all synthesized polymers, confirming the controllability of the polymer composition.

The molecular weight alters the swelling behavior and the mechanical properties of polymers. The molecular weight distributions of the polymers were measured by gel permeation chromatography in NMP, using polystyrene for calibration. The results are presented in Table 1. All molecular weight distribution curves are monomodal, suggesting no undesired side- or cross-linking reactions (see Figure S1). The synthesized polymers are soluble in DMSO, DMAc, and NMP and show sufficient film-forming properties. This allows the efficient preparation of thin membranes, resulting from the partially aromatic backbone and high molecular weight.[37,38]

Thermogravimetric analysis was performed in a temperature range between 30 and 900 °C. The results for BP-pTP0-Py and BP-pTP50-Py are displayed in Figure 3. An overview of all TGA curves can be found in the Supporting Information (see Figure S2).

Both polymers show outstanding thermal stability with onset temperatures above 300 °C, which agrees with the thermal stability reported for comparable chemical structures.[39] Slightly different thermal stability was observed when *p*-terphenyl was incorporated into the polymer structure. The onset temperature shifted slightly from 381 °C for BP-pTP0-Py to 392 °C for BP-pTP50-Py. In both cases, two distinct degradation regions can be observed between 400 and 500 °C and between 550 and 720 °C. For BP-pTP0-Py, the second region consists of one peak. For BP-pTP50-Py, a second peak is observable, which might result from the polymers' different backbone structures. To get further insight into the degradation mechanisms, the mass loss in the first degradation region was analyzed by deconvolution and analysis of the area below the peaks. It is assumed that the pyridine unit is degraded first.[40] The weight loss in the first degradation region and the theoretical weight loss for a C_5H_4N loss are given in Table S2. As can be seen, the weight loss is close to the theoretical weight for the split-off of one pyridine unit, supporting our hypothesis.

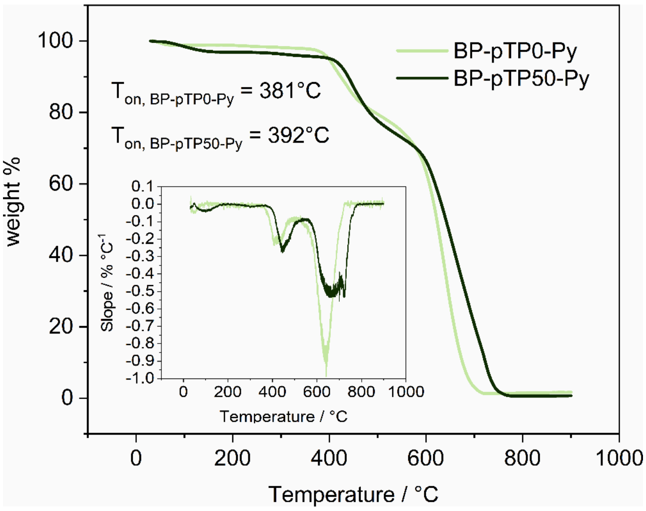

Figure 3. TGA thermograms of BP-pTP0-Py and BP-pTP50-Py between 30 and 900 °C with a heating rate of 20 K min^{-1} under synthetic air and curves of the first derivative of the TGA thermograms (inset). $T_{on, BP-pTPx-Py}$ are the onset temperatures.

3.2. Membrane Characterization.

From the above-mentioned polymers, membranes with dry thicknesses of around 15 to 20 μm were cast from NMP by the solution casting method, leading to flexible and transparent films both in wet and dry states. SEM images were recorded to analyze the surface homogeneity of the membranes. As can be seen from Figure S3, no signs of porosity or other defects are visible, proving the uniformity of the membranes. The absorption of acid plays a significant role in the performance of membranes for VRFB, as the electrolyte usually consists of vanadium salts dissolved in sulfuric acid. In addition, the novel membranes only work in acidic media due to the presence of non-quaternized pyridine groups, which get protonated and are thereby positively charged when immersed in the acidic electrolyte (Figure 1). The protonation increases the hydrophilicity of the material, allowing excess acid and water to enter the membrane.[41] In this regard, it is essential to mention that the overall liquid uptake and the composition of the absorbed liquid are crucial factors. Wan et al.[42] and Ikshan et al.[43] reported that for PBI-based membranes, the acid concentration within the membranes can substantially differ from that of the surrounding solution. Due to this, the swelling properties of the membranes were analyzed in 3 M sulfuric acid. The results are given in Table 2.

Generally, the swelling properties of membranes are influenced by a combination of different factors like IEC,[44]

Table 2. Swelling Properties of the Developed Membranes in 3 M H_2SO_4

material	theor. IEC[a] mmol g^{-1}	acid uptake [%]	acid concentration [mol L^{-1}]	area swelling [%]	thickness swelling [%]	ADL
FAPQ330	–[b]	32.9 ± 1.8	–[b]	24.4 ± 1.6	6.6 ± 1	–[b]
BP-pTP0-Py	3.07	85.0 ± 6.0	2.1 ± 0.2	43.5 ± 1.4	16.8 ± 8.5	1.33 ± 0.06
BP-pTP10-Py	3.00	84.5 ± 6.8	2.1 ± 0.1	42.3 ± 1.4	26.5 ± 5.5	1.34 ± 0.03
BP-pTP20-Py	2.94	77.2 ± 8.5	1.7 ± 0.2	36.7 ± 1.5	22.5 ± 2.2	1.26 ± 0.05
BP-pTP35-Py	2.84	62.0 ± 5.5	1.6 ± 0.1	32.5 ± 1.4	4.3 ± 1.3	1.18 ± 0.03
BP-pTP50-Py	2.75	63.0 ± 1.8	1.9 ± 0.2	32.5 ± 2.6	5.2 ± 0.8	1.22 ± 0.02

[a] Based on the mass of the deprotonated polymer. [b] No data are given as the membrane is unstable in KOH, and no detailed information about the composition and chemical structure of the material is available.

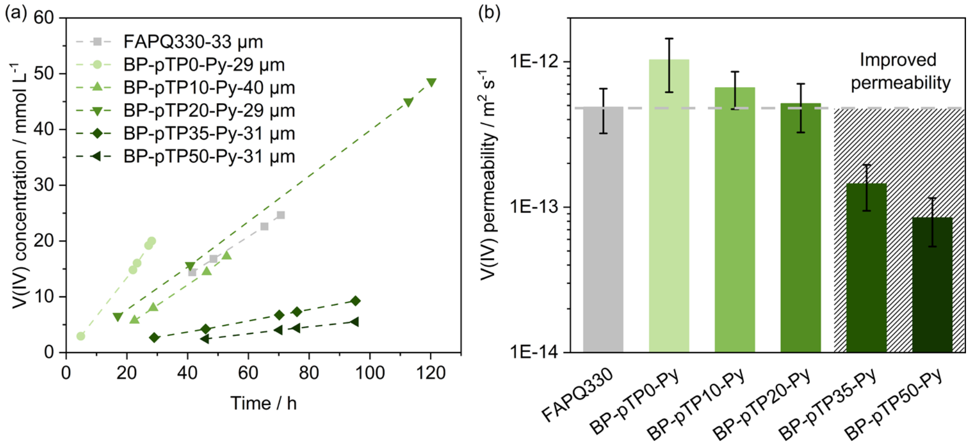

Figure 4. (a) V(IV) permeation tests and (b) V(IV) permeabilities of BP-pTPx-Py membranes (green) and FAPQ330 (gray). The dashed gray line marks the permeability of FAPQ330. Permeabilities are calculated from the slopes of the linear regression through the points in the V(IV) concentration vs time diagram. For all measurements, the coefficients of determination R^2 were ≥0.998 (compare Table S1). Error bars are the measurement uncertainties (p = 95%) based on the uncertainties of the slope of the linear regression through the points in the V(IV) concentration vs time diagram and the thickness measurement.

interchain distance,[43] and the extent of phase separation[45] of the polymer structure. In the case of the reported materials, the absorbed solution after immersion in sulfuric acid is comprised of bonded sulfuric acid through the protonation of the basic pyridine units and free acid and water, which are stored within the free volume.

With an increasing amount of *p*-terphenyl in the polymer structure, the overall acid uptake of the studied materials decreases because the *p*-terphenyl unit reduces the IEC and increases the hydrophobicity.[46] The reduced IEC leads to reduced uptake of bonded acid, whereas the increased hydrophobicity decreases free acid and water uptake. The reduction in overall acid uptake is particularly marked when the *p*-terphenyl content is increased from 20% to 35%.

A comparable drop with increasing *p*-terphenyl amounts can be observed for the ADL, although the difference between the membranes is not pronounced. The acid doping level of all membranes exceeds 1, meaning additional nonbonded acid is stored between the polymer chains. The ADL is slightly reduced by increasing the amount of *p*-terphenyl, possibly due to the increased hydrophobicity. In addition, biphenyl and terphenyl interact with themselves and with each other via the aromatic system. This might lead to distinct molecular interactions with different amounts of *p*-terphenyl. Furthermore, *p*-terphenyl increases the rigidity of the polymer backbone. Both effects can alter the overall morphology and interchain distance, impacting the swelling properties.[47−49]

Next to the already mentioned properties, the acid concentration also plays a crucial role in the performance of the membranes. Generally, two effects, the absorption of excess nonbound acid and the absorption of water, alter the acid concentration within the free volume of the membrane. Between 0% *p*-terphenyl and 35% *p*-terphenyl, a general trend to lower acid concentrations was observed, which can be explained by the decreasing excess acid uptake relative to the water uptake. However, for 50% *p*-terphenyl, this trend has not continued. By increasing the *p*-terphenyl amount from 35% to 50%, the overall weight gain and the amount of water per g membrane remained unchanged, whereas the amount of free acid per g membrane slightly increased (see Figure S4). One reason could be a change in morphology at a certain pTP content due to the rigidity of the pTP unit. Another might be a lower Donnan potential because of decreased fixed ion concentration within the membrane.[28,50]

Another important property is the thickness swelling of the membranes. The increased thickness, when immersed, leads to pressure-related forces within the cell, which can lead to leakages and cell failure. The thickness swelling values for the membranes with 0%, 10%, and 20% *p*-terphenyl are comparable. Significantly less thickness swelling was observed for the 35% and 50% pTP-containing membranes, presumably due to the lower overall acid uptake and less occupied volume than the other membranes.

Interestingly, BP-pTP35-Py and BP-pTP50-Py have much lower thickness swelling than the other membranes but only slightly lower area swelling. In general, the lower volume swelling should result in reduced vanadium crossover. The high anisotropy could further promote this trend if we assume that swelling in the thickness direction aligns the ion transport

Table 3. Tensile Properties of the Acid-Swollen Membranes at 23 °C and 61% RH

polymer	tensile strength [MPa]	Young's modulus [MPa]	elongation at break [%]	proportional limit stress [MPa]	proportional limit strain [%]
FAPQ330	21 ± 2	61 ± 4.9	130 ± 9.9	1.0 ± 0.25	1.7 ± 0.44
BP-pTP0-Py	11 ± 2	310 ± 110	14 ± 3.0	5.1 ± 1.4	2.1 ± 1.3
BP-pTP10-Py	17 ± 1	390 ± 26	29 ± 7.5	7.6 ± 0.59	2.3 ± 0.49
BP-pTP20-Py	20 ± 1	450 ± 50	29 ± 3.5	8.9 ± 0.66	2.3 ± 0.42
BP-pTP35-Py	22 ± 1	450 ± 40	48 ± 12	10 ± 0.52	2.7 ± 0.47
BP-pTP50-Py	22 ± 1	510 ± 30	32 ± 7.4	10 ± 2.0	2.3 ± 0.57

channels in the through-plane direction. The permeability data in Figure 4 agrees with these assumptions.

The crossover of vanadium species affects the CE and capacity during single-cell operation.[51] To minimize crossover energy losses, membranes must exhibit high $H^+/V(IV)$ selectivity. The V(IV) permeability through the membrane is usually characterized by a static crossover test utilizing an H-cell. After specific time intervals, the V(IV) concentration is measured. The results of the V(IV) permeation test for the membranes BP-pTP-x-Py and FAPQ330 are presented in Figure 4.

Compared to FAPQ330, the membranes BP-pTP0-Py, and BP-pTP10 show a slightly higher V(IV)-permeability, which might result from the high acid uptake compared to the other membranes. V(IV) transport through the membrane strongly depends on its morphology, especially when the chain-to-chain distances or channel diameters exceed the size of the hydrated V(IV) ions (ca. 0.7 nm).[37,52,53] The channel size of hydrated ion-exchange membranes is determined by the overall acid uptake and the molecular features of the polymer structure. For a polymer structure with hydrophilic moieties attached to the backbone by a C6 spacer, an average hydrophilic size of 3.0 nm has been reported.[54] The hydrophilic domain size of Nafion films was analyzed to be around 4 to 5 nm in size.[55] In this study, the polymer contains a pyridine unit separated from the backbone by a C1 spacer. Thus, the mobility of the functional unit is limited, which probably leads to inherently smaller ionic domains than in the previously mentioned cases. An increasing amount of *p*-terphenyl corresponds to lower V(IV)-permeabilities. Especially for BP-pTP35-Py and BP-pTP50, a drop in V(IV) permeabilities can be seen in Figure 4(b), resulting in lower permeabilities than the FAPQ330. A similar drop was also observed in the acid uptake values in Table 2, suggesting that the decrease in acid uptake is the main reason for this effect. Compared to recently published membranes based on polyhydroxyalkylations, the measured permeabilities of the novel membranes are in a comparable range between around 5×10^{12} m^2 s^{-1} and 5×10^{13} m^2 s^{-1}.[24,56]

As membranes for VRFB can experience mechanical stress during cell assembly or battery operation, the tensile properties of the acid-swollen membranes were analyzed. The results are presented in Table 3.

With increasing amounts of *p*-terphenyl, the tensile strength increases gradually. The effect is most significant between 0 mol % and 20 mol %. A similar trend can be observed for the Young's Modulus, which is the stress needed to increase the strain by 1% in the elastic region. The elongation at break is comparable for membranes BP-pTP10-Py, BP-pTP20-Py, and BP-pTP50-Py, whereas membrane BP-pTP0-Py shows a lower and BP-pTP35-Py a higher elongation at break. The proportional limit stress describes the amount of stress that can be applied until the membrane is irreversibly deformed. By raising the *p*-terphenyl content from 0 mol % to 35 mol %, the proportional limit stress can be doubled from 5 to 10 MPa. In conclusion, adding 20 mol % *p*-terphenyl leads to a distinct improvement in the tensile properties. Adding more than 20 mol % *p*-terphenyl only leads to minor improvements in the tensile strength. The comparison with the tensile properties of the FAPQ330 indicates that the FAPQ330 is a more flexible membrane and deforms plastically at lower loads, manifesting in high elongation, low proportional limit stress, and a significantly lower Young's Modulus.

The conductivity of the membrane corresponds to the VE of a VRFB and needs to be improved while maintaining the membrane's selectivity. Conductivity measurements were performed in 3 M H_2SO_4 and 1.5 M V(IV)/3 M H_2SO_4 solution to determine the conductivity in the absence and presence of vanadium ions. The results of the conductivity measurements and the $H^+/V(IV)$ selectivities are presented in Figure 5.

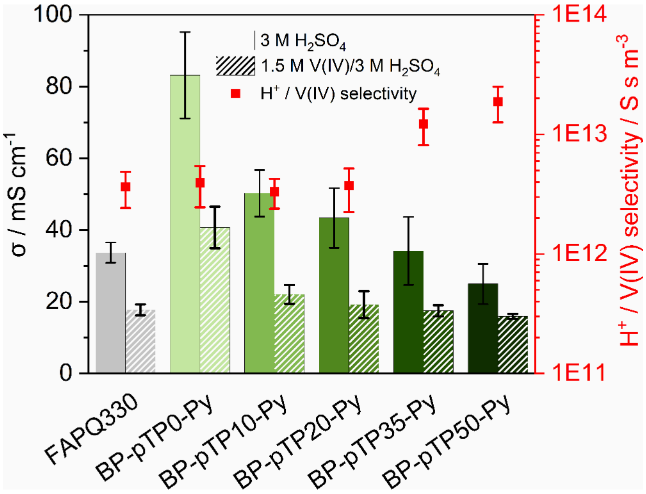

Figure 5. Conductivities σ and $H^+/V(IV)$ selectivities (red) of the novel developed membranes (green) and the reference membrane FAPQ330 (gray). Conductivity measurements in the presence of V(IV) are visualized with dashed columns. Errors bars are the standard deviations of three replicates. Selectivities were calculated from conductivities in 1.5 M V(IV)/3 M H_2SO_4 and the permeabilities presented in Figure 4.

A conductivity drop was observed for all membranes when immersed in an acidic V(IV) solution instead of sulfuric acid. This presumably results from vanadium species blocking the ion-conducting pathways and a lower sulfuric acid uptake due to the higher ionic strength of the surrounding solution.[57,58] The conductivity decreases with increasing amounts of *p*-terphenyl, which is a combined result of the decreasing IEC and reduced acid uptake due to the increased hydrophobicity of the polymer. The membranes with 0 mol %, 10 mol % and 20 mol % showed a significantly higher conductivity than the reference membrane FAPQ330. The membranes with 35 mol % and 50% mol showed similar or slightly lower conductivities. For the overall performance of a membrane, not only the conductivity but also the H^+/V-selectivity is crucial. As shown in Figure 5, BP-pTP0-Py, BP-pTP10-Py, and BP-pTP20-Py showed comparable selectivities to the FAPQ330. Only the membranes with 35 mol % and 50 mol % *p*-terphenyl exhibited higher H^+/V(IV)-selectivities than the reference membrane, corresponding to the significantly improved V(IV)-permeability but comparable conductivity.

Especially for the long-term operation of a VRFB battery, stability against the strongly oxidizing V(V) species is essential. In general, two scenarios regarding the degradation of ion exchange polymers must be considered. First, the chemical attack on the backbone can decrease molecular weight until the polymer becomes fragile. Second, the VO_2^+ can attack the functional group and transform it into a nonconductive moiety, gradually decreasing the membrane conductivity and VE of the cell. To determine the stability of the membranes, samples of BP-pTP0-Py and BP-pTP50-Py were placed into 1.6 M V(V)/2 M H_2SO_4 solution for 66 days at RT. The concentration of V(IV) in the test solution was determined by UV−vis spectroscopy. It is assumed that every V(IV) ion is the product of the oxidation reaction of the polymer and V(V). The results are given in Figure S5. For the FAPQ330 and both novel membranes, BP-pTP0-Py and BP-pTP50-Py, the V(IV) concentration in the immersion solution is in a comparable range. For BP-pTP0-Py, a slightly lower increase in the V(IV) concentration was recorded compared to BP-pTP50-Py and FAPQ330. This observation may result from the more extensive mesomeric system of terphenyl over biphenyl, which stabilizes potential transition states during the degradation reaction, thus favoring degradation reactions at *p*-terphenyl-containing sites in the polymer.[59] In addition to the UV−vis spectroscopic tracking of the V(IV) concentration, the molecular weight of the polymers was analyzed after the stability test. As shown in Figure 6, GPC measurements before and after the stability test revealed a slight molecular weight degradation for both novel materials, whereby the degradation is slightly more pronounced for BP-pTP50-Py compared to BP-pTP0-Py.

The comparison of the UV−vis spectroscopy and molecular weight determination results indicates an interconnection between the V(IV) concentration in corresponding solutions used for the ex-situ aging experiments and the extent of molecular weight degradation. For the membrane with higher *p*-terphenyl content, a greater amount of V(IV) was measured in the surrounding solution, and a more pronounced molecular weight degradation was measured, which supports our previously described hypothesis. Future research will focus on the analysis of the molecular weight degradation mechanism. To date, we are unaware of any research that has determined the molecular weight of polymers synthesized by PHA before and after the stability test.

In addition to the backbone stability, the intactness of the pyridine groups was analyzed by comparing the ^1H NMR spectra before and after the stability test. In Figure S6 and Figure S7, no changes in the signals corresponding to the pyridine units were noticeable, confirming the stability of the pyridine moieties. As both membranes showed minimal molecular weight degradation and exhibited no functional group degradation, the materials are considered stable under the tested conditions.

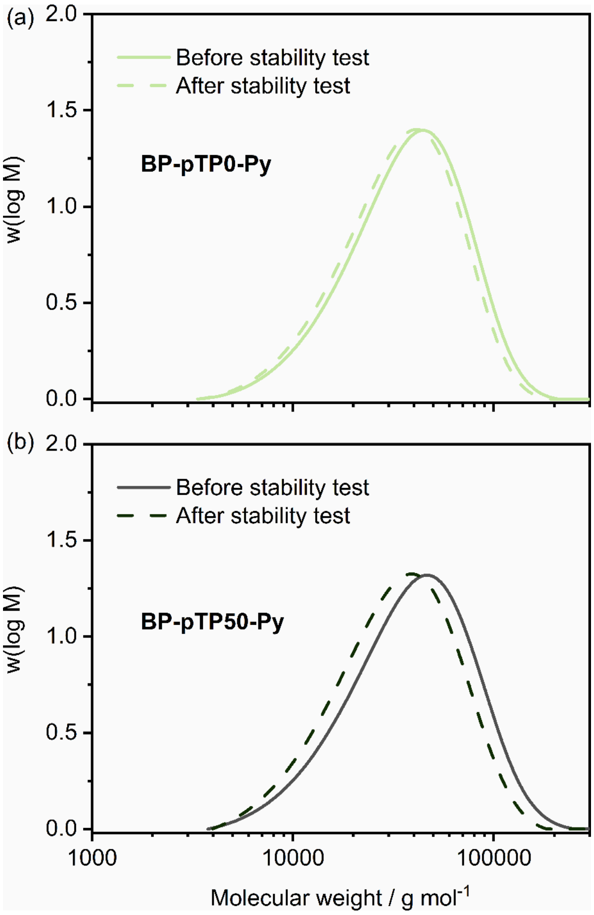

Figure 6. Molecular weight distribution of (a) BP-pTP0-Py (light green) and (b) BP-pTP50-Py (dark green) before (straight line) and after (dashed line) immersion in 1.6 M V(V)/2 M H_2SO_4 for 66 days.

In conclusion, the ex-situ characterization showed that the material properties could be tailored by changing the amount of pTP. An increase leads to improved mechanical properties, lower V(IV) permeability, lower conductivities, and a slightly increased molecular degradation rate. By carefully adjusting the pTP amount, it is possible to design membranes with higher ex-situ selectivity or significantly higher conductivity than the commercially available membrane FAPQ330, showing the versatility of the novel developed system. The membranes were further characterized in situ with VRFB single-cell tests based on the promising ex-situ results. The results are presented in the following chapter.

3.3. VRFB Single-Cell Tests.

The VRFB single-cell performance of the novel membranes and a reference membrane, FAPQ330, were evaluated at 50 mA cm^{-2}, 100 mA cm^{-2}, and 200 mA cm^{-2}. The averages of CE, VE, and EE for the ten cycles at each current density are presented in Figure 7. The CE, VE, and EE of every single cycle are given in Figures S8−S10, and the theoretical V(IV) crossover while charging based on the ex-situ V(IV) permeability in Table S3.

The CE is affected by parasitic side reactions and crossover of V-species.[60] The CEs of the novel membranes and the FAPQ330 are shown in Figure 7(a). The membranes with 20%, 35%, and 50% pTP show almost 99% CE. With a decreasing amount of pTP, lower CEs can be observed, resulting in a CE of 97.5% for BP-pTP0-Py-25 μm. One mechanism contributing to lower CE is the V(IV) diffusion

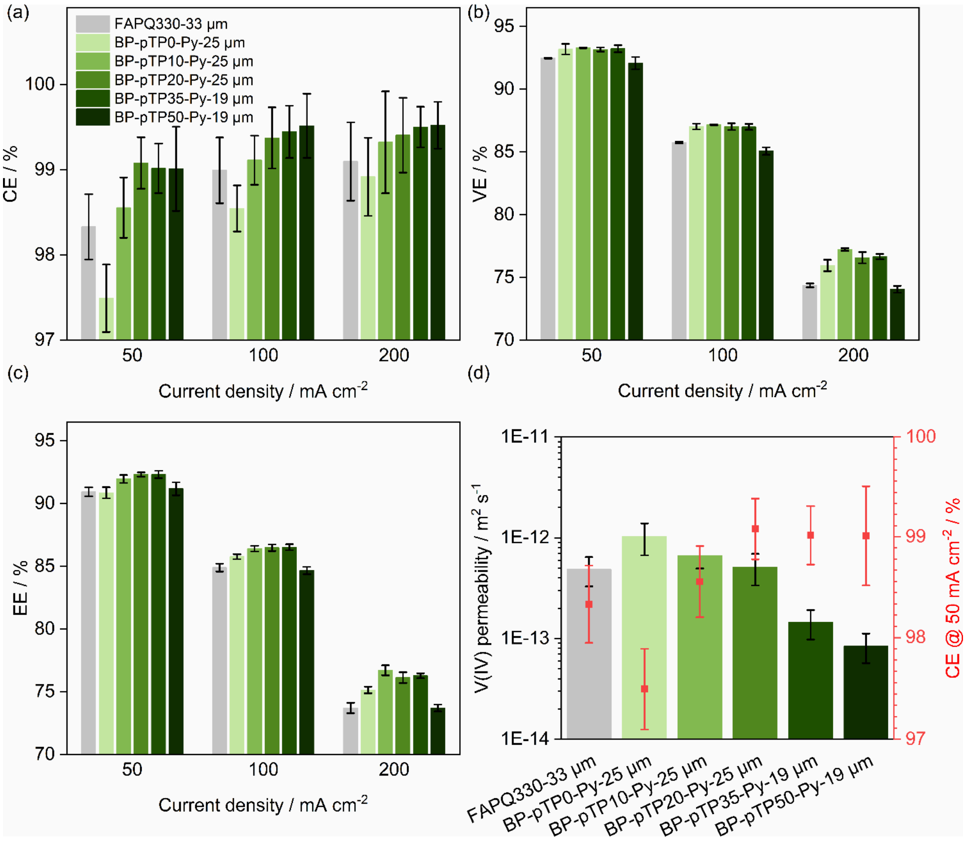

Figure 7. (a) CE, (b) VE, and (c) EE from VRFB single-cell tests at different current densities from cells equipped with the FAPQ330 (gray) and the novel developed membranes (green). The given data are the averages of 10 cycles at each current density. The error bars are the standard deviations of 10 cycles at each current density. (d) Correlation of the V(IV) permeability (black axis) and the CE at a current density of 50 mA cm^{-2} (red axis). Given thicknesses are the ex situ measured wet thicknesses of the membranes after immersion in the V electrolyte.

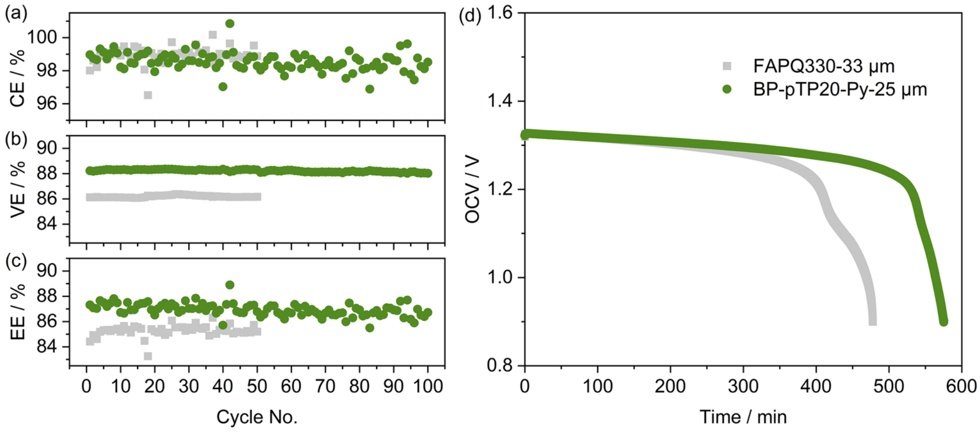

Figure 8. (a) CE, (b) VE, and (c) EE of FAPQ330 (gray) and BP-pTP20-Py (green) cycling tests at 100 mA cm^{-2} for 50 and 100 cycles, respectively. (d) Self-discharge test of FAPQ330 and BP-pTP20-Py starting from SOC = 20% down to a cell voltage of 0.9 V.

through the membrane (see Figure 4). The correlation of the V(IV)-permeability and the CE at 50 mA cm^{-2} is shown in Figure 7(d). As expected, a higher V(IV) permeability in the ex-situ test corresponds to a lower CE in the single-cell test, which can be associated with the membranes' swelling properties. In particular, BP-pTP35-Py and BP-pTP50-Py showed a comparatively low acid uptake (see Table 2), resulting in a high CE even at lower wet thicknesses of 19 μm compared to the 25 μm of the other developed membranes and 33 μm of the reference membrane FAPQ330.

The VEs at the different current densities are given in Figure 7(b). The cells equipped with the novel membranes showed slightly higher VE than those with the FAPQ330, except for BP-pTP50-Py, whose VE is slightly lower. At 50 mA cm^{-2} and 100 mA cm^{-2} no significant difference between the pyridine-containing membranes could have been observed except for BP-pTP50-Py, whose VE is slightly lower than the other membranes. At 200 mA cm^{-2}, BP-pTP10-Py showed the highest VE with 77.2%, which is significantly higher than the VE of the reference membrane FAPQ330 with 74.4%.

The EEs of the single cells using the novel developed membranes and the FAPQ330 are shown in Figure 7(c). Due to the similar VE, the membranes with high CEs at 50 mA cm^{-2} also show the highest EE at 50 mA cm^2. Especially the cells equipped with BP-pTP20-Py and BP-pTP35-Py showed significantly higher EE than the one with the FAPQ330 (92.3% vs 90.9%). With increasing current densities, the charging and discharging time is reduced, leading to higher CE. Thus, the EE at high current densities is mainly dominated by the VE and, therefore, by the ASR of the membrane.

Additionally, the discharge capacity retention was analyzed during the cycles of the single-cell tests (see Supporting Information S11−S13). For all cases, the discharge capacity retention remained above 96%. Only for BP-pTP0-Py at 50 mA cm^{-2}, the discharge capacity retention showed a strong trend toward lower capacities, which is probably connected to the high crossover of the membrane (high ex-situ permeability, low CE) and pronounced change in the electrolyte's composition.

As a result, the cell equipped with BP-pTP10-Py showed the highest EE of 76.7 at 200 mA cm^{-2}.

BP-pTP20-Py was selected for long-term cycling testing at 100 mA cm^{-2} due to its balanced properties in terms of CE and VE. Figure 8(a)−(c) shows the CE, VE, and EE during 50 cycles for the reference membrane FAPQ330 and during 100 cycles for BP-pTP20-Py. In both cases, no significant change in CE, VE, and EE can be observed, highlighting the stability of both membranes in terms of conductivity. The discharge capacity retentions during the cycling tests are given in Figure S14. In addition to the ex-situ V(IV) permeability test, the crossover properties of a VRFB membrane can also be determined by an in situ static self-discharge test. Single cells equipped with the FAPQ330 or BP-pTP20-Py were charged until SOC = 20% and then allowed to rest with deactivated pumps until an OCV of 0.9 V was reached. The corresponding results are presented in Figure 8(d). As can be seen, BP-pTP20-Py takes slightly longer to reach the threshold of 0.9 V. However, both discharge times are comparable, with slightly longer self-discharge time for BP-pTP20-Py. Therefore, the in situ results are consistent with those obtained in the ex-situ test, which showed similar crossover characteristics for the FAPQ330 and BP-pTP20-Py.

To conclude, the results above show that the system can easily be tailored for low or high-current-density applications. Increasing the pTP content leads to higher CE at low current densities, whereas with decreasing amounts of pTP, higher VE can be obtained at high current densities. Compared to other recently published membranes for VRFBs, BP-pTP20-Py, and BP-pTP35-Py achieved one of the highest EEs among materials with a CE exceeding 99% (see Figure S15).

4. CONCLUSION

A new versatile pyridine-containing polymer system with different IECs was developed, characterized ex-situ, and benchmarked in VRFB single-cell tests. The results show that the variation of the *p*-terphenyl content was a suitable approach to vary the physical properties of the membranes. The ^1H NMR spectra confirmed the expected structures and showed a high controllability of the copolymer composition. The novel polymers exhibited high thermal stability with an onset temperature of 381 °C. By varying the *p*-terphenyl content, the material properties can be optimized for high or low current density applications. At high current density (200 mA cm^{-2}), BP-pTP10-Py outperformed the FAPQ330 (73.7%) with an EE of 76.7%. At low current density (50 mA cm^{-2}), BP-pTP35-Py and BP-pTP50-Py showed the highest EE of 92.3% (vs 90.9% for the FAPQ330). BP-pTP20-Py showed balanced properties regarding conductivity and permeability and was analyzed in a long-term VRFB single-cell test, where no signs of degradation were observable. No functional group degradation and only minor molecular weight degradation were observed during the ex-situ stability tests. Further studies will be performed to analyze the underlying degradation mechanism.

■ ASSOCIATED CONTENT

Supporting Information

The Supporting Information is available free of charge at https://pubs.acs.org/doi/10.1021/acsaem.4c01671.

Additional experimental data, including GPC curves, TGA curves, SEM images, ^1H NMR spectra, and supporting data of the VRFB single-cell tests (DOCX)

■ AUTHOR INFORMATION

Corresponding Authors

Julian Stonawski − *Forschungszentrum Jülich GmbH, Helmholtz Institute Erlangen-Nürnberg for Renewable Energy (IET-2), 91058 Erlangen, Germany; Department of Chemical and Biological Engineering, Friedrich-Alexander-Universität Erlangen-Nürnberg, 91058 Erlangen, Germany;* orcid.org/0009-0003-0062-9925; Email: j.stonawski@fz-juelich.de, stonawski.julian@web.de

Dirk Henkensmeier − *Hydrogen·Fuel Cell Research Center, Korea Institute of Science and Technology (KIST), Seoul 02792, South Korea; Energy & Environment Technology, KIST School, University of Science and Technology (UST), Seoul 02792, South Korea;* orcid.org/0000-0003-2330-953X; Email: henkensmeier@kist.re.kr

Authors

Melanie Schroeder − *J. Schmalz GmbH, 72293 Glatten, Germany*

Janett Gördes − *J. Schmalz GmbH, 72293 Glatten, Germany*

Frieder Junginger − *Electrochemical Energy Systems, IMTEK − Department of Microsystems Engineering, University of Freiburg, 79110 Freiburg, Germany*

Linus Hager − *Forschungszentrum Jülich GmbH, Helmholtz Institute Erlangen-Nürnberg for Renewable Energy (IET-2), 91058 Erlangen, Germany; Department of Chemical and Biological Engineering, Friedrich-Alexander-Universität Erlangen-Nürnberg, 91058 Erlangen, Germany*

Pascal Lauf − *Forschungszentrum Jülich GmbH, Helmholtz Institute Erlangen-Nürnberg for Renewable Energy (IET-2), 91058 Erlangen, Germany; Department of Chemical and Biological Engineering, Friedrich-Alexander-Universität Erlangen-Nürnberg, 91058 Erlangen, Germany*

Muhammad Mara Ikhsan − *Hydrogen·Fuel Cell Research Center, Korea Institute of Science and Technology (KIST), Seoul 02792, South Korea; Energy & Environment Technology, KIST School, University of Science and Technology (UST), Seoul 02792, South Korea*

Simon Thiele − *Forschungszentrum Jülich GmbH, Helmholtz Institute Erlangen-Nürnberg for Renewable Energy (IET-2), 91058 Erlangen, Germany; Department of Chemical and Biological Engineering, Friedrich-Alexander-Universität*

Erlangen-Nürnberg, 91058 Erlangen, Germany; orcid.org/0000-0002-4248-2752

Jochen Kerres − *Forschungszentrum Jülich GmbH, Helmholtz Institute Erlangen-Nürnberg for Renewable Energy (IET-2), 91058 Erlangen, Germany; Faculty of Natural Science, North-West University, Potchefstroom 2520, South Africa;* orcid.org/0000-0003-4972-6307

Complete contact information is available at: https://pubs.acs.org/10.1021/acsaem.4c01671

Author Contributions

J.S.: Conceptualization, methodology, investigation, visualization, validation, formal analysis, data curation, writing—original draft. M.S.: Investigation, writing—review and editing. J.G.: Investigation. F.J.: Investigation. L.H.: Writing—review and editing. P.L.: Visualization, writing—review and editing. M.M.I.: Writing—review and editing. D.H.: Supervision, writing—review and editing. S.T.: Supervision, writing—review and editing. J.A.K.: Supervision, conceptualization, writing—review and editing, funding acquisition.

Funding

This project has been funded by the German Federal Ministry for Economic Affairs and Climate Action (BMWK, funding number: 03EI3018B). This project received funding from KIST internal project (2E33281).

Notes

The authors declare no competing financial interest.

REFERENCES

(1) Akinyele, D. O.; Rayudu, R. K. Review of energy storage technologies for sustainable power networks. *Sustainable Energy Technol. Assess.* **2014**, *8*, 74−91.

(2) Zhao, H.; Wu, Q.; Hu, S.; Xu, H.; Rasmussen, C. N. Review of energy storage system for wind power integration support. *Appl. Energy* **2015**, *137*, 545−553.

(3) Arévalo-Cid, P.; Dias, P.; Mendes, A.; Azevedo, J. Redox flow batteries: a new frontier on energy storage. *Sustain. Energy Fuels* **2021**, *5* (21), 5366−5419.

(4) Li, Z.; Jiang, T.; Ali, M.; Wu, C.; Chen, W. Recent progress in organic species for redox flow batteries. *Energy Storage Mater.* **2022**, *50*, 105−138.

(5) Lee, S.; Kim, M.; Park, J.; Choi, J.; Kang, J.; Park, M. A high voltage aqueous zinc-vanadium redox flow battery with bimodal tin and copper clusters by a continuous-flow electrometallic synthesis. *ACS Appl. Mater. Interfaces* **2023**, *15* (5), 7002−7013.

(6) Aluko, A.; Knight, A. A review on vanadium redox flow battery storage systems for large-scale power systems application. *IEEE Access* **2023**, *11*, 13773−13793.

(7) Sun, C.; Zhang, H. Review of the development of first-generation redox flow batteries: iron-chromium system. *ChemSusChem* **2022**, *15* (1), No. e202101798.

(8) Rodby, K. E.; Carney, T. J.; Ashraf Gandomi, Y.; Barton, J. L.; Darling, R. M.; Brushett, F. R. Assessing the levelized cost of vanadium redox flow batteries with capacity fade and rebalancing. *J. Power Sources* **2020**, *460*, 227958.

(9) Lin, C.-H.; Chien, M.-Y.; Chuang, Y.-C.; Lai, C.-C.; Sun, Y.-M.; Liu, T.-Y. Porous membranes of polysulfone and graphene oxide nanohybrids for vanadium redox flow battery. *Polymers* **2022**, *14* (24), 5405−5418.

(10) Che, X.; Zhao, H.; Ren, X.; Zhang, D.; Wei, H.; Liu, J.; Zhang, X.; Yang, J. Porous polybenzimidazole membranes with high ion selectivity for the vanadium redox flow battery. *J. Membr. Sci.* **2020**, *611*, 118359−118368.

(11) Düerkop, D.; Widdecke, H.; Schilde, C.; Kunz, U.; Schmiemann, A. Polymer membranes for all-vanadium redox flow batteries: a review. *Membranes* **2021**, *11* (3), 214−267.

(12) Gubler, L. Membranes and separators for redox flow batteries. *Curr. Opin. Electrochem.* **2019**, *18*, 31−36.

(13) Darling, R. M.; Saraidaridis, J. D.; Shovlin, C.; Fortin, M.; Murdock, L. A.; Benicewicz, B. C. The influence of current density on transport of vanadium cations through membranes with different charges. *J. Electrochem. Soc.* **2021**, *168* (4), 040516−040523.

(14) Chu, J.; Liu, Q.; Ji, W.; Li, J.; Ma, X. Novel microporous sulfonated polyimide membranes with high energy efficiency under low ion exchange capacity for all vanadium flow battery. *Electrochim. Acta* **2023**, *446*, 142080.

(15) Zhai, L.; Zhu, Y.-L.; Wang, G.; He, H.; Wang, F.; Jiang, F.; Chai, S.; Li, X.; Guo, H.; Wu, L.; Li, H. Ionic-nanophase hybridization of nafion by supramolecular patching for enhanced proton selectivity in redox flow batteries. *Nano Lett.* **2023**, *23* (9), 3887−3896.

(16) Salmeron-Sanchez, I.; Mansouri Bakvand, P.; Shirole, A.; Ramón Avilés-Moreno, J.; Ocón, P.; Jannasch, P.; Wreland Lindström, R.; Khataee, A. Zwitterionic poly(terphenylene piperidinium) membranes for vanadium redox flow batteries. *Chem. Eng. J.* **2023**, *474*, 145879.

(17) Wang, Z.; Ren, J.; Sun, J.; Li, Y.; Guo, Z.; Liu, B.; Fan, X.; Zhao, T. The anion conductivity of acid-doped polybenzimidazole membrane and utilization in mitigating the capacity decay of vanadium redox flow battery stacks. *Chem. Eng. J.* **2023**, *474*, 145621.

(18) Gubler, L.; Vonlanthen, D.; Schneider, A.; Oldenburg, F. J. Composite membranes containing a porous separator and a polybenzimidazole thin film for vanadium redox flow batteries. *J. Electrochem. Soc.* **2020**, *167* (10), 100502.

(19) Zhang, B.; Zhao, M.; Liu, Q.; Zhang, X.; Fu, Y.; Zhang, E.; Wang, G.; Zhang, Z.; Yuan, X.; Zhang, S. High performance membranes based on pyridine containing poly (aryl ether ketone ketone) for vanadium redox flow battery applications. *J. Power Sources* **2021**, *506*, 230128.

(20) Noh, C.; Jung, M.; Henkensmeier, D.; Nam, S. W.; Kwon, Y. Vanadium redox flow batteries using meta-polybenzimidazole-based membranes of different thicknesses. *ACS Appl. Mater. Interfaces* **2017**, *9* (42), 36799−36809.

(21) Zhang, B.; Yang, Z.; Liu, Q.; Liu, Y.; Fu, Y.; Zhang, X.; Jiang, S.; Zhang, X.; Zhang, E.; Wang, K.; Wang, G.; Zhang, Z.; Zhang, S. Swelling-induced cross-linked pyridine-containing membranes with high stability and conductivity for vanadium redox flow batteries. *ACS Sustainable Chem. Eng.* **2023**, *11* (31), 11601−11612.

(22) Colquhoun, H. M.; Zolotukhin, M. G.; Khalilov, L. M.; Dzhemilev, U. M. Superelectrophiles in aromatic polymer chemistry. *Macromolecules* **2001**, *34* (4), 1122−1124.

(23) Khataee, A.; Nederstedt, H.; Jannasch, P.; Lindström, R. W. Poly(arylene alkylene)s functionalized with perfluorosulfonic acid groups as proton exchange membranes for vanadium redox flow batteries. *J. Membr. Sci.* **2023**, *671*, 121390.

(24) Mu, T.; Tang, W.; Jin, Y.; Che, X.; Liu, J.; Yang, J. Ether-free poly(p-terphenyl-co-acetylpyridine) membranes with different thicknesses for vanadium redox flow batteries. *ACS Appl. Energy Mater.* **2022**, *5* (9), 11713−11722.

(25) Lin, C.; Cheng, W.; Miao, X.; Shen, X.; Ling, L. Clustered piperidinium-functionalized poly(terphenylene) anion exchange membranes with well-developed conductive nanochannels. *J. Colloid Interface Sci.* **2022**, *608*, 1247−1256.

(26) Rezayani, M.; Sharif, F.; Makki, H. Understanding ion diffusion in anion exchange membranes; effects of morphology and mobility of pendant cationic groups. *J. Mater. Chem. A* **2022**, *10* (35), 18295−18307.

(27) Wang, Y.; Wang, Y.; Guo, M.; Ban, T.; Zhu, X. High performance poly(isatin alkyl-terphenyl)s proton exchange membranes with flexible alkylsulfonated side groups. *High Perform. Polym.* **2022**, *34* (7), 797−810.

(28) Kushner, D. I.; Crothers, A. R.; Kusoglu, A.; Weber, A. Z. Transport phenomena in flow battery ion-conducting membranes. *Curr. Opin. Electrochem.* **2020**, *21*, 132−139.

(29) Kawase, M.; Teshima, M.; Saito, S.; Tani, S. Trifluoroacetylation of methylpyridines and other methylazines: a convenient access to trifluoroacetonylazines. *Heterocycles* **1998**, *48* (10), 2103.

(30) Wang, J.; Zhao, Y.; Setzler, B. P.; Rojas-Carbonell, S.; Ben Yehuda, C.; Amel, A.; Page, M.; Wang, L.; Hu, K.; Shi, L.; Gottesfeld, S.; Xu, B.; Yan, Y. Poly(aryl piperidinium) membranes and ionomers for hydroxide exchange membrane fuel cells. *Nat. Energy* **2019**, *4* (5), 392−398.

(31) Cruz-Rosado, A.; Romero-Hernández, J. E.; Ríos-López, M.; López-Morales, S.; Cedillo, G.; Ríos-Ruiz, L. M.; Cetina-Mancilla, E.; Palacios-Alquisira, J.; Zolotukhin, M. G.; Vivaldo-Lima, E. Molecular weight development in the superacid-catalyzed polyhydroxyalkylation of 1-propylisatin and biphenyl at stoichiometric conditions. *Polymer* **2022**, *243*, 124616.

(32) Gou, W. W.; Gao, W. T.; Gao, X. L.; Zhang, Q. G.; Zhu, A. M.; Liu, Q. L. Highly conductive fluorinated poly(biphenyl piperidinium) anion exchange membranes with robust durability. *J. Membr. Sci.* **2022**, *645*, 120200.

(33) Min, K.; Chae, J. E.; Lee, Y.; Kim, H.-J.; Kim, T.-H. Crosslinked poly(m-terphenyl N-methyl piperidinium)-SEBS membranes with aryl-ether free and kinked backbones as highly stable and conductive anion exchange membranes. *J. Membr. Sci.* **2022**, *653*, 120487.

(34) Ren, R.; Zhang, S.; Miller, H. A.; Vizza, F.; Varcoe, J. R.; He, Q. Facile preparation of novel cardo Poly(oxindolebiphenylylene) with pendent quaternary ammonium by superacid-catalysed polyhydroxyalkylation reaction for anion exchange membranes. *J. Membr. Sci.* **2019**, *591*, 117320.

(35) Qian, J.; Cai, S.; Hu, J.; Wang, C.; Li, G. Preparation and properties of quaternary ammonium anion exchange membranes with flexible side chains for the vanadium redox flow battery. *Ind. Eng. Chem. Res.* **2023**, *62* (6), 2719−2728.

(36) Chu, X.; Liu, J.; Miao, S.; Liu, L.; Huang, Y.; Tang, E.; Liu, S.; Xing, X.; Li, N. Crucial role of side-chain functionality in anion exchange membranes: Properties and alkaline fuel cell performance. *J. Membr. Sci.* **2021**, *625*, 119172.

(37) Kumao, R.; Miyatake, K. Sulfonated and fluorinated aromatic terpolymers as proton conductive membranes: synthesis, structure, and properties. *Bull. Chem. Soc. Jpn.* **2022**, *95* (5), 707−712.

(38) Nunes, R. W.; Martin, J. R.; Johnson, J. F. Influence of molecular weight and molecular weight distribution on mechanical properties of polymers. *Polymer Engineering & Sci.* **1982**, *22* (4), 205−228.

(39) Jin, Y.; Wang, T.; Che, X.; Dong, J.; Li, Q.; Yang, J. Poly(arylene pyridine)s: New alternative materials for high temperature polymer electrolyte fuel cells. *J. Power Sources* **2022**, *526*, 231131.

(40) Azhari, S. J.; Diab, M. A. Thermal degradation and stability of poly(4-vinylpyridine) homopolymer and copolymers of 4-vinylpyridine with methyl acrylate. *Polym. Degrad. Stab.* **1998**, *60* (2−3), 253−256.

(41) Stewart-Sloan, C. R.; Olsen, B. D. Protonation-induced microphase separation in thin films of a polyelectrolyte-hydrophilic diblock copolymer. *ACS Macro Lett.* **2014**, 3 (5), 410−414.

(42) Wan, L.; Xu, Z.; Wang, P.; Lin, Y.; Wang, B. H2SO4-doped polybenzimidazole membranes for hydrogen production with acid-alkaline amphoteric water electrolysis. *J. Membr. Sci.* **2021**, *618*, 118642.

(43) Mara Ikhsan, M.; Abbas, S.; Do, X. H.; Choi, S.-Y.; Azizi, K.; Hjuler, H. A.; Jang, J. H.; Ha, H. Y.; Henkensmeier, D. Polybenzimidazole membranes for vanadium redox flow batteries: Effect of sulfuric acid doping conditions. *Chem. Eng. J.* **2022**, *435*, 134902.

(44) Guler, E.; Zhang, Y.; Saakes, M.; Nijmeijer, K. Tailor-made anion-exchange membranes for salinity gradient power generation using reverse electrodialysis. *ChemSusChem* **2012**, *5* (11), 2262−2270.

(45) Zhang, K.; Yu, W.; Ge, X.; Wu, L.; Xu, T. Molecular dynamics insight into phase separation and transport in anion-exchange membranes: Effect of hydrophobicity of backbones. *J. Membr. Sci.* **2022**, *661*, 120922.

(46) Lee, W.-H.; Park, E. J.; Han, J.; Shin, D. W.; Kim, Y. S.; Bae, C. Poly(terphenylene) anion exchange membranes: The effect of backbone structure on morphology and membrane property. *ACS macro letters* **2017**, *6* (5), 566−570.

(47) Finkelmann, H.; Happ, M.; Portugal, M.; Ringsdorf, H. Liquid crystalline polymers with biphenyl-moieties as mesogenic group. *Makromol. Chem.* **1978**, *179* (10), 2541−2544.

(48) Shah, R. A.; Ostertag, T. W.; Tang, S.; Dziubla, T. D.; Hilt, J. Z. Development of biphenyl monomers and associated crosslinked polymers with intramolecular pi-pi interactions. *J. Appl. Polym. Sci.* **2021**, *138* (16), 50257.

(49) Bishop, R. New aspects of aromatic $\pi\cdots\pi$ and CH$\cdots\pi$ interactions in crystal engineering. In *The Importance of Pi-Interactions in Crystal Engineering*; Tiekink, E. R. T., Zukerman-Schpector, J., Eds.; Wiley, 2012; pp 41−77.

(50) Aydogan Gokturk, P.; Sujanani, R.; Qian, J.; Wang, Y.; Katz, L. E.; Freeman, B. D.; Crumlin, E. J. The Donnan potential revealed. *Nat. Commun.* **2022**, *13* (1), 5880.

(51) Loktionov, P.; Pustovalova, A.; Pichugov, R.; Konev, D.; Antipov, A. Quantifying effect of faradaic imbalance and crossover on capacity fade of vanadium redox flow battery. *Electrochim. Acta* **2024**, *485*, 144047.

(52) Yan, X. H.; Zhou, X. L.; Zhao, T. S.; Jiang, H. R.; Zeng, L. A highly selective proton exchange membrane with highly ordered, vertically aligned, and subnanosized 1D channels for redox flow batteries. *J. Power Sources* **2018**, *406*, 35−41.

(53) Kreuer, K.-D.; Münchinger, A. Fast and selective ionic transport: from ion-conducting channels to ion exchange membranes for flow batteries. *Annu. Rev. Mater. Res.* **2021**, *51* (1), 21−46.

(54) Hager, L.; Hegelheimer, M.; Stonawski, J.; Freiberg, A. T. S.; Jaramillo-Hernández, C.; Abellán, G.; Hutzler, A.; Böhm, T.; Thiele, S.; Kerres, J. Novel side chain functionalized polystyrene/O-PBI blends with high alkaline stability for anion exchange membrane water electrolysis (AEMWE). *J. Mater. Chem. A* **2023**, *11* (41), 22347−22359.

(55) Porat, Z.; Fryer, J. R.; Huxham, M.; Rubinstein, I. Electron Microscopy Investigation of the Microstructure of Nafion Films. *J. Phys. Chem.* **1995**, *99* (13), 4667−4671.

(56) Mu, T.; Tang, W.; Shi, N.; Wang, G.; Wang, T.; Wang, T.; Yang, J. Novel ether-free membranes based on poly(p-terphenylene methylimidazole) for vanadium redox flow battery applications. *J. Membr. Sci.* **2022**, *659*, 120793.

(57) Lee, W.; Jung, M.; Serhiichuk, D.; Noh, C.; Gupta, G.; Harms, C.; Kwon, Y.; Henkensmeier, D. Layered composite membranes based on porous PVDF coated with a thin, dense PBI layer for vanadium redox flow batteries. *J. Membr. Sci.* **2019**, *591*, 117333.

(58) Lee, Y.; Kim, S.; Hempelmann, R.; Jang, J. H.; Kim, H.-J.; Han, J.; Kim, J.; Henkensmeier, D. Nafion membranes with a sulfonated organic additive for the use in vanadium redox flow batteries. *J. Appl. Polym. Sci.* **2019**, *136* (21), 47547.

(59) Kalenchuk, A. N.; Koklin, A. E.; Bogdan, V. I.; Kustov, L. M. Hydrogenation of biphenyl and isomeric terphenyls over a Pt-containing catalyst. *Russ. Chem. Bull.* **2017**, *66* (7), 1208−1212.

(60) Qian, X.; Jung, H.-Y.; Jung, S. A comprehensive study of parasitic gas evolution reactions in a vanadium redox flow battery. *J. Cleaner Prod.* **2023**, *428*, 139468.